


 Cite this: *RSC Adv.*, 2025, **15**, 50766

## A theoretical investigation on the photochemical performance of hybrid dye-sensitized solar cells based on Keggin-type polyoxometalates

 Maryam Fallah, Bahram Yadollahi  \* and Reza Omidyan

Polyoxometalates (POMs) are versatile inorganic compounds that can be integrated into hybrid materials due to their unique properties, which allow them to interact effectively with organic components. In this study, we designed a series of donor-acceptor (D-A) type hybrids in which dithieno[3,2-*b*:2',3'-*d*]pyrrole (DTP)-derived building blocks served as donors and the Keggin-type POM acted as the acceptor moiety. The electronic structures, UV-visible absorption spectra, and photovoltaic properties of these hybrid compounds, along with their potential applications in n-type dye-sensitized solar cells, were investigated using density functional theory (DFT) and time-dependent DFT methods. Key parameters such as excitation energies ( $E_{\text{ver}}$ ), maximum absorption wavelengths ( $\lambda_{\text{max}}$ ), oscillator strengths ( $f$ ), charge-transfer percentages, local excitation percentages, and  $\Delta r$  values for the principal molecular orbitals were systematically computed. To better understand intramolecular charge-transfer processes, natural transition orbitals and the charge density differences between the excited state and the ground state were analyzed. Research shows that among the 12 designed hybrid compounds, TD/POM, SN5/POM, DTP/POM, and DBTP/POM exhibited the highest  $\Delta r$  and CT charge values, making them the most effective sensitizers for dye-sensitized solar cells due to their superior LHE and high  $V_{\text{OC}}$ .

 Received 15th September 2025  
 Accepted 20th November 2025

 DOI: 10.1039/d5ra06975k  
[rsc.li/rsc-advances](http://rsc.li/rsc-advances)

### Introduction

The energy crisis, one of the most pressing challenges of the current world, has led to a higher demand for alternative energy sources. Solar energy has emerged as a preferred choice due to its eco-friendly nature and ability to be converted into electricity using the photovoltaic effect.<sup>1,2</sup> There has been a significant focus on dye-sensitized solar cells (DSSCs) due to their potential benefits, such as affordability and simple manufacturing compared to silicon and other inorganic semiconductor-based solar devices.<sup>3</sup> A DSSC mainly comprises a semiconductor material, an electrolyte, and a dye sensitizer. Considering the vital role of the dye in DSSCs, substantial efforts have been focused on enhancing power conversion efficiencies by designing and synthesizing various dyes.<sup>4</sup> In 1991, Grätzel and colleagues made significant advancements in dye-sensitized solar cells by utilizing a titanium oxide ( $\text{TiO}_2$ ) electrode coated with a monolayer of dye molecules, achieving a notable efficiency of 7%.<sup>5</sup> To enhance the light-harvesting capacity of sensitizers, it is crucial to adjust molecular configurations to broaden the range and strength of sunlight absorption. Thus, researchers have embarked on various endeavors to synthesize and explore different sensitizers, aiming to further improve the power conversion efficiency of these solar cells.<sup>6</sup>

Polyoxometalates (POMs) are transition metal oxide clusters composed of  $d^0$  or  $d^1$  metal ions interconnected by oxygen atoms. They have been extensively studied, and numerous POMs have been synthesized using metals such as Mo, W, V, and Nb.<sup>7,8</sup> They exhibit a wide range of structural diversity, and due to their remarkable electronic characteristics, POMs show great promise in diverse fields, such as catalysis, medicine, biology, and optics.<sup>9,10</sup> Moreover, POMs can accept and transfer electrons while maintaining structural integrity, making them highly valuable in photovoltaics.<sup>11</sup> Research findings suggest that the distinctive redox stability of the Keggin structure enables certain POMs within this family to accommodate up to 24 electrons. Keggin-type  $[\text{XM}_{12}\text{O}_{40}]^{n-}$  clusters can undergo reduction by 12 electrons. This has been substantiated through both theoretical and experimental investigations, facilitating their application in battery cathodes.<sup>12</sup>

POMs can serve as inorganic components for creating hybrid materials with organic constituents. This combination allows for synergistic interactions between POMs and organic compounds, improving the overall properties and functionalities of the produced materials.<sup>13,14</sup> The introduction of organic species to the POM clusters leads to significant  $d$ - $\pi$  interaction between the delocalized  $\pi$ -electrons of the organic molecules and the  $d$ -electrons of the cluster. Compared to the organic segments or POMs alone, the POM-based organic-inorganic hybrids experience a redshift in their UV-vis absorption spectra.<sup>15</sup> Studies indicated that POM utilization enhances the

Department of Chemistry, University of Isfahan, Isfahan 81746-73441, Iran. E-mail:  
[yadollahi@chem.ui.ac.ir](mailto:yadollahi@chem.ui.ac.ir); [yadollahi.b@gmail.com](mailto:yadollahi.b@gmail.com)



photoelectron efficiency of DSSCs.<sup>16,17</sup> The broad UV-vis absorption exhibited by heteropolyblues (HPBs) can enhance sunlight absorption in DSSCs. The UV-vis absorption and energy levels of HPBs can be altered by the presence of enriched electrons, allowing for easier transfer to the conduction band of  $\text{TiO}_2$ . Moreover, enriched electrons in HPBs can serve as electron repositories, potentially modifying the electronic structure of the POM molecules. These modifications are of immediate significance, particularly when POMs are employed as sensitizers or co-sensitizers in DSSCs.<sup>18,19</sup>

Thiophene is a fundamental electron-donating component in constructing conjugated materials due to its ease of synthesis and superior performance. However, its inter-annular single bonds allow for rotation, decreasing the planarity between the neighbouring thiophene units and potentially impacting the material's properties.<sup>20–22</sup> Incorporating heteroatoms within the connecting region of the adjacent thiophene rings to create diverse fused tricyclic structures can optimize planarity. This optimization increases the alignment of the  $\pi$  orbitals, facilitating more efficient conjugation along the backbone.<sup>23</sup> Dithieno[3,2-*b*:2',3'-*d*] pyrrole (DTP) moieties have garnered significant interest due to the presence of an electron-rich nitrogen atom, enhancing stability in the oxidized state and reducing the bandgap. Many researchers have reported numerous building blocks derived from the DTP backbone, showcasing their innovative modifications.<sup>24</sup>

Quantum chemical theoretical calculations provide a valuable approach for systematically examining the energy levels, electron density, structure, and stability of POMs. Density functional theory (DFT) is crucial for developing and producing novel functional POMs. For example, Poblet *et al.* employed the DFT approach for evaluating the energy levels of the highest occupied molecular orbitals (HOMO) and lowest unoccupied molecular orbitals (LUMO) in Keggin-type POMs.<sup>25</sup> Therefore, theoretical computations play a crucial role in developing novel, efficient POM-based, organic–inorganic hybrid dyes for DSSCs.<sup>26</sup> This study focuses on the theoretical examination of twelve specifically designed donor–acceptor (D–A) hybrids (briefly DTP/POM) consisting of dithieno[3,2-*b*:2',3'-*d*] pyrrole (DTP)-based building blocks and a Keggin-type POM ( $[\text{PW}_{12}\text{O}_{40}]^{3-}$ ). Density functional theory (DFT) and time-dependent DFT (TDDFT) analyses were conducted for assessing the geometrical configurations, the electronic characteristics, the absorption spectra, the nature of transitions, and the charge-transfer (CT) properties of the synthesized compounds. Ultimately, we aim to investigate the potential applications of hybrid compounds based on Keggin-type POMs as dyes in DSSCs.

## Experimental

### Computational methods

The quantum-chemical computations of the structures were carried out with the scientific software, Gaussian16. The geometries of all the dyes with a Cs symmetry were optimized based on the density functional theoretical method using the B3LYP functional (charge = –3 and multiplicity = 1), a hybrid

approach combining Becke's three-parameter method with the Lee–Yang–Parr correlation functional.<sup>27</sup> The standard 6-31G(d) polarized double- $\xi$  basis set was used for the atoms O, C, N, S, and H, while the W atom was characterized using the effective core potential (ECP) double- $\xi$  (DZ) basis set of LanL2DZ to account for relativistic effects. According to the optimized ground-state geometries using the B3LYP method, the TD-DFT calculations were conducted with the hybrid functional CAM-B3LYP. The transition metal W was modeled using the LanL2DZ basis set, while the nonmetal elements used the 6-31G(d) all-electron basis set for TD-DFT calculations. All designed structures underwent optimization using the Gaussian 16 software package,<sup>28</sup> with default convergence criteria. Specifically, the following thresholds were applied: maximum force: 0.00045 hartree per bohr, root-mean-square (RMS) force: 0.00030 hartree per bohr, maximum displacement: 0.0018 Bohr, RMS displacement: 0.0012 bohr; these criteria correspond to the “tight” convergence criteria used by default in Gaussian 16 for geometry optimizations. It is important to highlight that the B3LYP functional, when utilized with augmented LANL2DZ basis sets, accurately reproduces the experimental spectrum of the Keggin anions.<sup>29</sup> We selected the B3LYP functional due to its consistently reliable performance, as demonstrated in both our previous studies and those conducted by other research groups.<sup>30–32</sup>

Since in different studies on POMs acetonitrile has been selected as the solvent, the influence of the solvent was considered by utilizing the polarizable continuum model (PCM) based on acetonitrile solution.<sup>33</sup> The electron densities for the ground and excited states of the dyes were calculated and visualized using Multiwfn 3.8 software.<sup>34</sup>

## Results and discussion

### Molecular structures

During recent years, significant advancements have been achieved in the studying of DTP-based building blocks. The DTP-based polymers and the small molecules that have been documented primarily consist of the original DTP unit or *N*-aryl DTP. These blocks can be categorized into four distinct types: (1) basic building blocks including DTP, *N*-acyl DTP, and pyrrolo[3,2-*d*:4,5-*d*']bisthiazole (PBTz); (2) fused DTP building blocks, such as pyrrole-modified pentathiophene (NPTA) and dithieno[3,2-*d*:2',3'-*d*']thieno[3,2-*b*:2',3'-*b*]dipyrrole (DTDP), or so-called S,N-heteropentacenes (SN5) and S,N-heterohexacenes (SN6); (3) lactam building blocks like dithieno[3,2-*b*:2',3'-*d*]pyridin-5(4*H*)-one (DTPO), [7,7'-bidithieno[3,2-*b*:2',3'-*d*]pyridine]-5,5'(4*H*,4'*H*)-dione (BDTP), and [7,7'-bidithieno[3,2-*b*:2',3'-*d*]pyridine]-5,5'(4*H*,4'*H*)-dione (TD); and (4) imide building blocks, including *N*-alkyl-2,2'-bithiophene-3,3'-dicarboximide (BTI) and [2-(thiophen-2'-yl)-5-(thiophen-2''-yl)thieno[3,2-*b*]-thiophene-3,3':6,3''-bis(dicarboximide)] (TBI).<sup>24</sup> To compare with X-ray crystallography information for the  $[\text{PW}_{12}\text{O}_{40}]^{3-}$  system,<sup>25</sup> geometry optimization of the  $[\text{PW}_{12}\text{O}_{40}]^{3-}$  species was performed *via* two methods, using the B3LYP/6-31G(d)/LanL2DZ and PBE/6-31G(d)/LanL2DZ levels in the singlet spin state. For  $[\text{PW}_{12}\text{O}_{40}]^{3-}$ , the predictions suggest that the



singlet spin state ( $S = 0$ ) represents the most stable configuration. In contrast, earlier theoretical studies conducted by our team revealed that the triplet ( $S = 1$ ) and quintet ( $S = 2$ ) spin states are 57.30 and 125.50 kcal mol<sup>-1</sup> higher in energy than the singlet state, respectively.<sup>35</sup> Selected optimized geometry parameters for  $[\text{PW}_{12}\text{O}_{40}]^{3-}$  in the singlet spin state are tabulated in Table S1. As indicated in Table S1, the theoretical geometric parameters obtained using B3LYP aligned more closely with the respective experimental values compared to those derived from the PBE method. Consequently, the geometries of all the dyes were optimized utilizing the B3LYP/6-31G(d)/LANL2DZ method.

Initially, the geometry of DTP, the twelve designed hybrids incorporating the Keggin-type POM, and the DTP-based building blocks were optimized using the B3LYP/6-31G\* computational method. In the Fig. 1 and S1, the optimized molecular structures of the designed hybrids (Fig. 1), DTP, and DTP/POM (Fig. S1) are depicted (refer to the SI file). The computed HOMO and LUMO of DTP and DTP/POM in the ground state are illustrated in Fig. 2.

The analysis of Fig. 2 reveals that the HOMO and LUMO of DTP can be primarily assigned as the local  $\pi$ - $\pi^*$  characters. In contrast, the HOMO of DTP-POM exhibits  $\pi$ -electron delocalization from the DTP component to the W atom *via* the

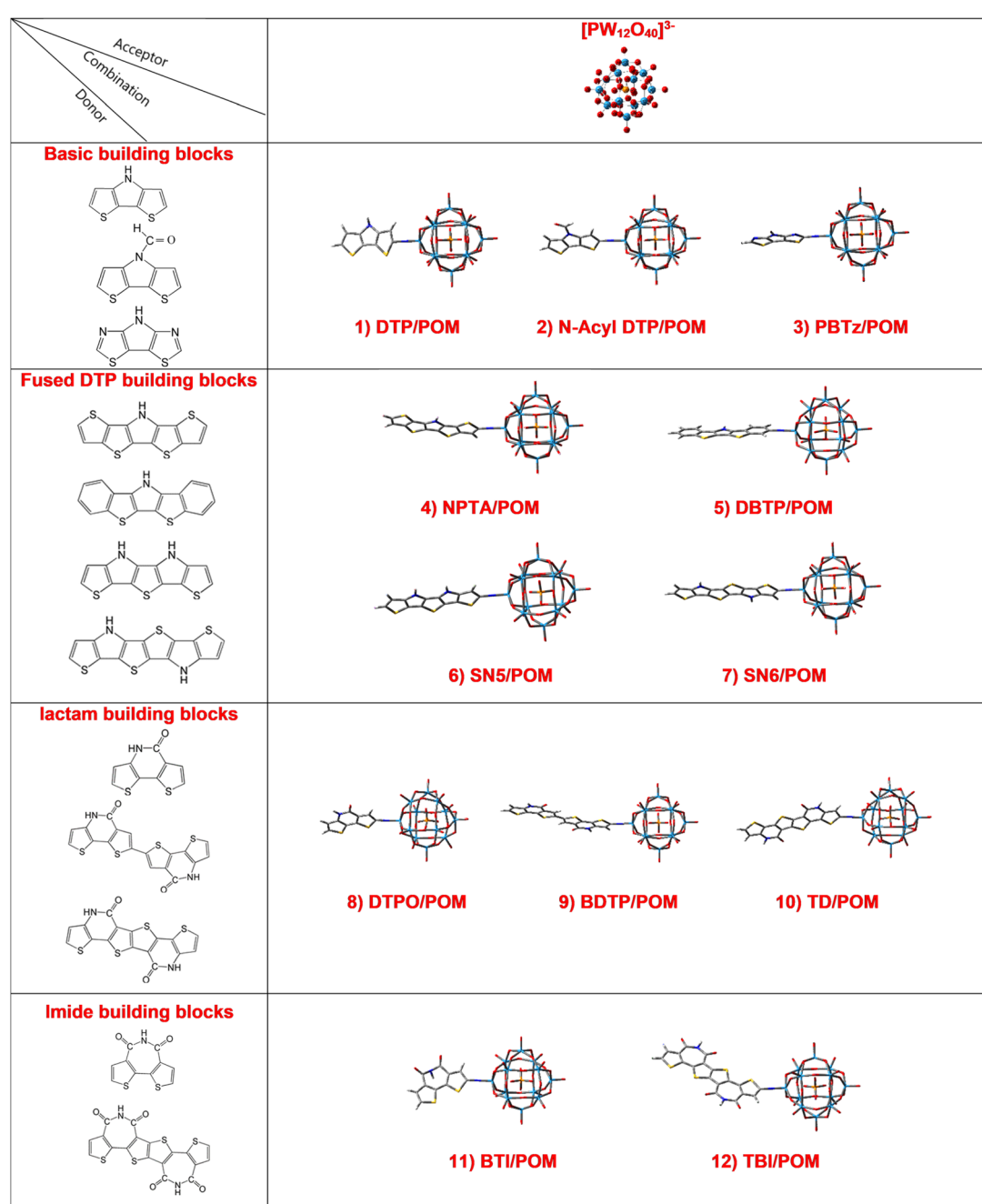


Fig. 1 Optimized molecular structures of the studied designed hybrids.



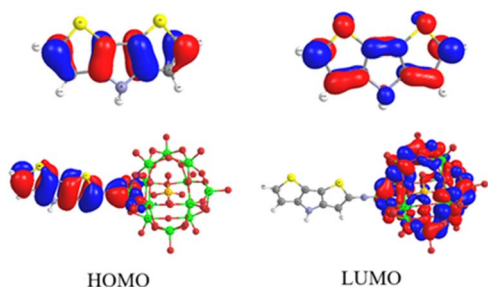


Fig. 2 The HOMO and LUMO orbitals of DTP (top) and DTP-POM (bottom) determined at the 6-31G(d) theoretical model.

bonding N atom, while the LUMO is confined to the POM segment. The delocalized  $\pi$ -bond is characterized by a d-p  $\pi$ -bond formed between the  $p_y$  orbital of the N atom and the  $d_{yz}$  orbital of the W atom, which is connected to the N atom. This  $\pi$ -bond is associated with the DTP segment, indicating significant electronic interaction between the DTP unit and the POM components.

The impact of the frontier molecular orbital (FMO) distributions on how dyes absorb light and transition between energy states is well acknowledged. Frontier molecular orbitals (MOs) for systems 1–12 were determined at the SCF/6-31G\* theoretical level. As shown in Fig. S2 (refer to the SI file), the LUMO, LUMO+1, LUMO+2, LUMO+3, and LUMO+4 are localized on the POM cluster, while LUMO+5 was predicted to arise from a combination of the  $\pi^*$  orbital of DTP and the d orbitals of W in POM.

### Vertical electronic transition energies

Concerning absorption, it is important to note that the conventional exchange–correlation functional—whether pure or hybrid—significantly underestimate the excitation energies of the states with pronounced CT character, primarily due to a self-interaction error.<sup>36</sup> A novel density functional, known as the Coulomb-attenuated hybrid exchange–correlation

functional (CAM-B3LYP), has been recently introduced to address these limitations. It has demonstrated the capability to accurately predict molecular CT spectra.<sup>37</sup> The CAM-B3LYP (Coulomb-Attenuating Method B3LYP) improves upon the B3LYP functional by incorporating a long-range correction into the exchange–correlation functional, which enhances the depiction of long-range interactions.<sup>38</sup>

To assess the impact of the POM on the photophysical characteristics of the investigated dyes, the UV-vis absorption spectra of the dyes were simulated at the CAM-B3LYP/6-31G(d)/LANL2DZ level, in the default acetonitrile solvent (based on the PCM algorithm of the Gaussian 16 program). For the TD-DFT calculation, 15 excited states were computed to derive the absorption spectra. The calculated transition energies (eV), mainly contributed to the MOs in electronic transitions, and the oscillator strength ( $f$ ) for the selected electronic transitions are tabulated in Table S2 (refer to the SI file). Among the presented electronic states, those located within the visible spectrum and exhibiting the highest oscillator strengths were chosen. Additionally, the CT character, local excitation (LE) characters, and  $\Delta r$  values for the principal molecular orbital transitions are presented in Table 1.

The  $\Delta r$  parameter reflects the charge centroids of the orbitals involved in the excitation, providing insight into the nature of the transition. This parameter can be interpreted in terms of the spatial separation between a hole and an electron. Valence excitations are generally associated with shorter distances, while CT excitations tend to correspond to longer distances.<sup>39,40</sup>

The information provided in Table 1 reveals that the synthesized dyes, SN6/POM and BDTP/POM, possess significant oscillator strengths ( $f$ ). However, DTP/POM, DBTP/POM, SN5/POM, and TD/POM show the highest possibility of a CT. Consequently, a more comprehensive analysis of the photophysical characteristics of these substances was performed. The examination of the CT% and LE% values for the compounds indicates that the ratios of CT% to LE% for NPTA/POM and SN6/POM were approximately the same at 52/48. In contrast, the

Table 1 Electronic transition states, main MO transition,  $\lambda_{\max}^a$ ,  $f^b$ ,  $E_{\text{ver}}^c$ ,  $^d\text{CT}\%$ ,  $^e\text{LE}\%$ , and  $\Delta r^f$  of the designed hybrids

Entry	Dye	State	Main Mo transition	$\lambda_{\max}$ (nm)	$f$	$E_{\text{ver}}$ (eV)	CT (%)	LE (%)	$\Delta r$ (Å)
1	<b>DTP/POM</b>	<b><math>S_4</math></b>	<b><math>H \rightarrow L + 5 (50\%)</math></b>	<b>431</b>	<b>0.9</b>	<b>2.88</b>	<b>75</b>	<b>25</b>	<b>7.55</b>
2	<i>N</i> -Acyl DTP/POM	$S_3$	$H \rightarrow L + 5 (87\%)$	421	1.46	2.68	52	48	3.45
3	PBTz/POM	$S_3$	$H \rightarrow L + 5 (88\%)$	424	1.37	2.93	57	43	3.76
4	NPTA/POM	$S_3$	$H \rightarrow L + 5 (85\%)$	462	1.99	2.58	52	48	5.19
5	<b>DBTP/POM</b>	<b><math>S_3</math></b>	<b><math>H \rightarrow L + 4 (34\%)</math></b>	<b>425</b>	<b>0.78</b>	<b>3.16</b>	<b>73</b>	<b>27</b>	<b>9.67</b>
6	<b>SN5/POM</b>	$S_3$	$H \rightarrow L + 5 (72\%)$	480	1.7	2.58	58	42	6.02
		<b><math>S_4</math></b>	<b><math>H \rightarrow L + 4 (37\%)</math></b>	<b>477</b>	<b>0.4</b>	<b>2.60</b>	<b>76</b>	<b>24</b>	<b>9.58</b>
7	<b>SN6/POM</b>	$S_3$	$H \rightarrow L + 5 (81\%)$	486	2.31	2.55	52	48	6.14
8	DTPO/POM	$S_3$	$H \rightarrow L + 5 (85\%)$	428	1.53	2.89	53	47	3.81
9	<b>BDTP/POM</b>	<b><math>S_2</math></b>	<b><math>H \rightarrow L + 5 (77\%)</math></b>	<b>474</b>	<b>2.1</b>	<b>2.61</b>	<b>40</b>	<b>60</b>	<b>6.29</b>
10	<b>TD/POM</b>	$S_2$	$H \rightarrow L + 5 (74\%)$	464.5	1.82	2.67	46	54	6.09
		$S_3$	$H \rightarrow L (50\%)$	<b>460</b>	<b>0.2</b>	<b>2.69</b>	<b>82</b>	<b>18</b>	<b>11.09</b>
11	BTI/POM	$S_2$	$H \rightarrow L + 5 (92\%)$	438	1.00	2.83	29	71	1.09
12	TBI/POM	$S_1$	$H \rightarrow L + 5 (80\%)$	474	1.88	2.61	33	67	3.20

<sup>a</sup>  $\lambda_{\max}$  = maximum absorption wavelengths. <sup>b</sup>  $f$  = oscillator strengths. <sup>c</sup>  $E_{\text{ver}}$  = calculated excitation energies. <sup>d</sup> CT% = charge-transfer excitation percentage. <sup>e</sup> LE% = local excitation percentage. <sup>f</sup>  $\Delta r$  = charge-transfer length.



ratios for DTP/POM, DBTP/POM, SN5/POM, and TD/POM were 75/25, 73/27, 76/24, and 82/18, respectively. These results imply that, in these particular dyes, the CT component was significantly greater than LE. Notably, the  $\Delta r$  values for DTP/POM, DBTP/POM, SN5/POM, SN6/POM, BDTP/POM, and TD/POM were greater than those of the other dyes.

The transfer of an electron in a dye from the electron donor to the electron acceptor upon excitation is crucial. NTOs offer a more concise representation of excitations compared to canonical orbitals and thus they are considered as a useful method for electron-transfer analysis.<sup>41</sup> The accompanying plots for the NTOs are illustrated in Fig. S3 (refer to the SI file). Although the diagrams illustrate that the hole is situated within the organic moieties, and the electron is predominantly concentrated on the  $\pi^*$  of the organic moieties and the POM group in all the designed hybrids, there is a notable distinction among these four structures.

As stated above, among the synthesized dyes, two were selected due to their higher oscillator strengths, and four were selected due to their higher CT character for closer evaluation.

Their charge density difference (CDD) between their excited state and their ground state is illustrated in Table 2. In this map, the isovalue was set to 0.002; green and blue correspond to an increase and decrease of the excited-state density, respectively, relative to the ground-state density. The centroid can be calculated to reveal the most representative positions of the hole and electron distributions. The  $C_{\text{hole}}$  and  $C_{\text{ele}}$  map was used for facilitating the visual study of the holes and electrons. The spatial separation between the centroid of the hole and electron ( $\Delta r$ ), along with the extent of overlap between the hole and the electron ( $S_r$ ) for the six compounds is also shown in Table 2.

The analysis of the  $S_r$  values indicates that the overlap of holes and electrons in compounds DTP/POM, TD/POM, SN5/POM, and DBTP/POM was significantly lower compared to compounds SN6/POM and BDTP/POM. This could suggest an improved separation of the hole–electron pairs within these compounds. The indices of the other studied designed hybrids, such as CDD, the  $C_{\text{hole}}$  &  $C_{\text{ele}}$  map,  $\Delta r$ ,  $S_r$ , and  $t_{\text{index}}$ , and  $E_{\text{coul}}$  for the six compounds is also shown in Table S3 (refer to the SI file), which demonstrates that

**Table 2** The CDD<sup>a</sup>,  $C_{\text{hole}}$  and  $C_{\text{ele}}$  map<sup>b</sup> (green and blue show hole and electron respectively),  $\Delta r$ ,  $S_r$ <sup>c</sup>,  $D_{\text{index}}$ <sup>d</sup>,  $t_{\text{index}}$ <sup>e</sup>, and  $E_{\text{coul}}$ <sup>f</sup> for two compounds with the highest oscillator strength and four compounds with the highest CT percentage

Compound	CDD	$C_{\text{hole}}$ & $C_{\text{ele}}$ map	$\Delta r$ (Å)	$S_r$ (a.u)	$D_{\text{index}}$	$t_{\text{index}}$	$E_{\text{coul}}$ (eV)
DTP/POM			7.55	0.16	7.08	4.87	2.15
DBTP/POM			9.67	0.52	6.52	2.63	2.48
SN5/POM (S4)			9.58	0.37	7.14	4.42	2.04
SN6/POM			6.143	0.75	2.93	-0.12	2.9
BDTP/POM			6.29	0.79	2.286	-1.32	3.04
TD/POM (S3)			11.09	0.30	8.23	4.74	2.02

<sup>a</sup> CDD = charge density difference. <sup>b</sup>  $C_{\text{hole}}$  &  $C_{\text{ele}}$  map = graph of the distance between the center of the hole and the electron. <sup>c</sup>  $S_r$  = overlap between the hole and the electron. <sup>d</sup>  $D_{\text{index}}$  = hole–electron distance. <sup>e</sup>  $t_{\text{index}}$  = separation degree of hole and electron in CT direction. <sup>f</sup>  $E_{\text{coul}}$  = hole–electron Coulomb attraction energy.



the overlap between the holes and electrons exceeded 0.7. We subsequently analyzed the intramolecular charge-transfer (ICT) parameters across these six compounds (Fig. 3). The process of ICT occurs when the absorption of light transfers an electron from a donor to an acceptor, influencing the formation of charge-separated states. Effective ICT is essential for achieving high efficiency in photovoltaic conversion. To evaluate the possibility of ICT, critical parameters were computed using the Multiwfn program. The extended values of  $\Delta r$  and  $d_{CT}$  signify the maximal degree of electron transfer, which plays a crucial role in enhancing the overall efficiency through effective ICT.

Various ICT parameters were calculated for assessing the ICT capabilities of dyes, including the quantity of transferred charges ( $q_{CT}$ ), the effective charge-transfer distance ( $d_{CT}$ ), and the  $t_{index}$ , which evaluates the separation degree between  $\rho^+(r)$  and  $\rho^-(r)$  based on the total densities of both the ground and excited states.

As Fig. 3 illustrates, the calculated value of  $d_{CT}$  follows the order: TD/POM ( $d_{CT} = 8.23 \text{ \AA}$ ) > SN5/POM ( $d_{CT} = 7.14 \text{ \AA}$ ) > DTP/POM ( $d_{CT} = 7.08 \text{ \AA}$ ) > DBTP/POM ( $d_{CT} = 6.52 \text{ \AA}$ ) > SN6/POM ( $d_{CT} = 2.93 \text{ \AA}$ ) > BDTP/POM ( $d_{CT} = 2.29 \text{ \AA}$ ). TD/POM, SN5/POM, DTP/POM, and DBTP/POM exhibit a larger distance between the center of the hole and the electron compared to SN6/POM and BDTP/POM. This increased distance resulted in reduced overlap between the holes and electrons in these compounds.

The term  $q_{CT}$  refers to the overall quantity of charge distribution affected during electron excitation; it does not indicate a net transfer of charge between different fragments, such as from a donor group to an acceptor group. The data in Fig. 2 indicate that the six analyzed compounds exhibited nearly identical  $q_{CT}$  values; however, TD/POM and BDTP/POM demonstrated elevated  $q_{CT}$  levels.

The  $t$  index reflects the hole–electron separation in the CT direction. A  $t_{index} < 0$  implies that the hole and electron are not substantially separated due to CT. As illustrated in Fig. 3, SN6/POM and BDTP/POM exhibit a negative  $t_{index}$ , suggesting that the separation of electrons and holes did not occur. In contrast, TD/POM, SN5/POM, DTP/POM, and DBTP/POM demonstrate distinct separation of distributions, as indicated by their positive  $t$  indices. This phenomenon may be attributed to a higher CT% relative to LE%.

To achieve high-energy conversion efficiency, it is essential for the electron and hole pairs to dissociate into distinct positive and negative charges, thereby avoiding recombination

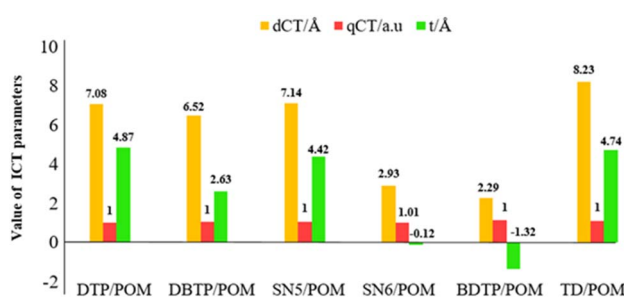


Fig. 3 Key ICT parameters of the studied dyes.

Table 3 Contribution of fragments to holes and electrons<sup>a</sup>

Fragment	Hole (%)	Electron (%)
DTP	62	0
N	13	0
POM	25	100

<sup>a</sup> Transferred electrons between fragments. DTP to N: 0.00, N to DTP: 0.00, and net DTP to N: 0.00. **DTP to POM: 0.62, POM to DTP: 0.00, and net DTP to POM: 0.62.** N to POM: 0.13, POM to N: 0.00, and net N to POM: 0.13.

caused by coulombic attraction. This dissociation process necessitates overcoming the binding energy, implying that the dye molecules must exhibit a lower exciton binding energy to facilitate effective energy conversion.<sup>42</sup> The hole–electron coulomb attraction energy of the dyes was calculated and is given in Table 3. The larger the  $D_{index}$ , the farther the distance between the main distribution regions of the holes and electrons, and thus the weaker the coulomb attractive energy. From the data, it was found that the coulomb attraction energies of TD/POM, SN5/POM, DTP/POM, and DBTP/POM were among the smallest compared to SN6/POM and BDTP/POM.

To enhance the investigation of the electron-transfer characters, each compound was segmented into three distinct components: (1) the organic portion, (2) the nitrogen atom (bridge), and (3) the inorganic component (POM). The composition of these fragments concerning holes and electrons can be represented as a heat map, effectively illustrating their distribution characteristics. Consequently, the contributions of each fragment to the holes and electrons using a heat map were analyzed. Fig. 4 illustrates the heat map along with an analysis of the transitions occurring between the designated fragments for DTP/POM. The heat maps for DBTP/POM, SN5/POM, SN6/POM, BDTP/POM, and TD/POM are displayed in Fig. S4 (refer to the SI file).

As illustrated in Fig. 4 and Table 3, in DTP/POM, the predominant contribution to electron donation (62%) was attributed to the organic component, whereas the POM component was solely responsible for 100% of electron

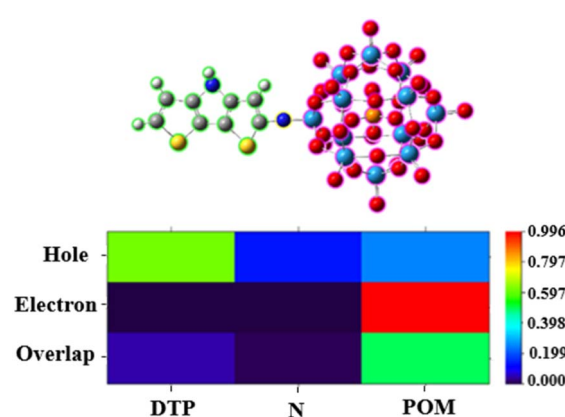


Fig. 4 The DTP/POM heat map.



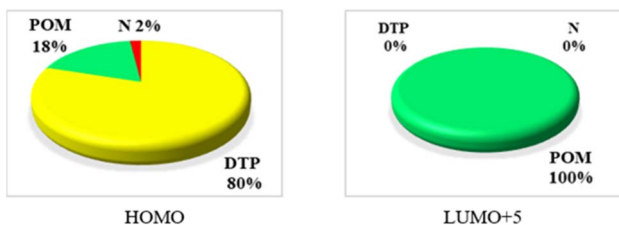


Fig. 5 Percentage of each fragment to the molecular orbitals of DTP/POM.

acceptance. The nitrogen bonding atom contributes to merely 13% of the electron donation. A comparison of the heat map for the other five hybrids reveals that the contributions of the organic and inorganic components in hybrids DBTP/POM, SN5/POM, and TD/POM were identical, while in hybrids SN6/POM and BDTP/POM, the organic component exhibited the greatest contribution as both an electron donor and an electron acceptor.

An examination of the electron transfers among the identified fragments suggests ligand-to-metal charge transfer (LMCT) processes. For SN6/POM and BDTP/POM, the proportion of the organic component in the electron was greater than that of the POMs. Furthermore, the electron transfers revealed two distinct mechanisms: LLCT (ligand-to-ligand charge transfer) and LMCT.

Fig. 5 illustrates the contribution of each fragment to the molecular orbitals engaged in the absorption spectrum for DTP/POM. The participation magnitude of each fragment for various compounds is detailed in Fig. S5 (SI file). As shown, the dye component contributes over 80% to the HOMOs, while the POM predominantly influences the LUMOs(+n). Notably, in DTP/POM, DBTP/POM, SN5/POM, and TD/POM, the POM's proportion in the LUMOs(+n) is significantly greater compared to SN6/POM and BDTP/POM.

### The performance of designed systems in DSSC

**Energy levels of systems.** Concerning the mechanism of n-type DSSCs, it has been established that the LUMO energy level of the dye should be higher than the conduction band (CB) edge of semiconductor ( $E_{CB}\text{TiO}_2 = -4.0$  eV).<sup>43</sup> This configuration facilitates an efficient photo-induced charge injection from the excited sensitizers to the CB of  $\text{TiO}_2$ . Additionally, the HOMO energy level of the sensitizers is positioned lower than the  $\text{I}^-/\text{I}_3^-$  redox level, ensuring effective dye regeneration.<sup>44</sup> Fig. 6 illustrates the FMOs and HOMO-LUMO (H-L) gaps for the systems. It is evident that the LUMO energy levels of these systems are consistently more positive than the CB edge energy of  $\text{TiO}_2$ , while the HOMO energy levels are more negative than the  $\text{I}^-/\text{I}_3^-$  redox potential. This alignment meets the requirements for dyes utilized in n-DSSCs. The LUMO energies appear to be somewhat similar, whereas the HOMO energies show slight variations.

**Optoelectronic properties.** The short-circuit current density ( $J_{sc}$ ) plays a crucial role in determining the power conversion efficiency (PCE) of a system. This factor is directly proportional

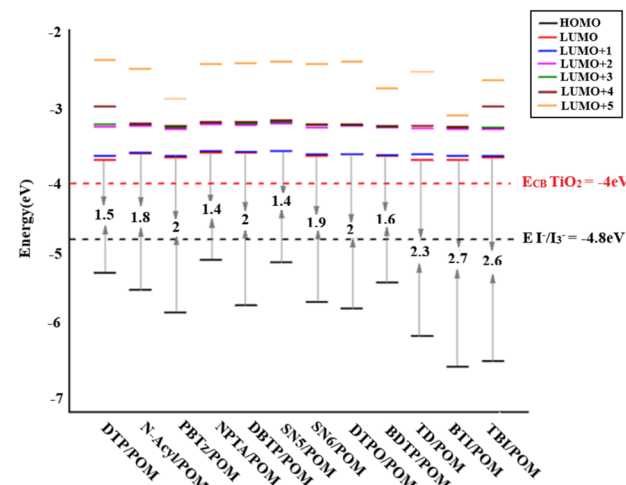


Fig. 6 Frontier molecular orbital energy levels of systems.

to both the light-harvesting efficiency (LHE) and the electron injection efficiency ( $\varphi_{\text{inject}}$ ). The LHE indicates the dye's capacity to absorb or utilize photons from sunlight. Consequently, a high LHE is crucial for the effective performance of a dye sensitizer in DSSCs. A negative  $\Delta G_{\text{inject}}$  facilitates a smooth electron injection process. Subsequently, the oxidized dye underwent reduction through an electron transfer from  $\text{I}^{3-}$ . This reduction process was closely associated with  $\Delta G_{\text{reg}}$ , which was further enhanced by a negative  $\Delta G_{\text{reg}}$ . Nevertheless, if the reduction reaction fails to complete within the lifetime of charge separation, the reduced dye can recombine with the  $\text{TiO}_2$  electron. This phenomenon was assessed by  $\Delta G_{\text{cr}}$ ; specifically, a positive  $\Delta G_{\text{cr}}$  signifies that the charge recombination process is non-spontaneous. Consequently, the combination of a large LHE, negative  $\Delta G_{\text{inject}}$ ,  $\Delta G_{\text{cr}}$ , and positive  $\Delta G_{\text{reg}}$  supports a robust light-harvesting capability, providing an adequate driving force for efficient electron injection and dye regeneration, and mitigating the charge recombination process.<sup>45</sup>

To illustrate the influence of donor and acceptor groups on the  $J_{sc}$  of DSSC, the UV-visible absorption spectra of the dyes were analyzed. The calculated parameters are presented in Table 4. The  $E_{\text{OX}}^{\text{dye}}$  is evaluated using Koopman's theorem, which relates to the negative value of the HOMO energy. According to eqn S11–S18,  $E_{\text{OX}}^{\text{dye}}$ , LHE,  $\Delta G_{\text{inject}}$ ,  $\Delta G_{\text{reg}}$ ,  $\Delta G_{\text{cr}}$  and  $V_{\text{OC}}$  for the studied designed hybrids were determined and analyzed.

The data indicate that the LHE values for the examined dye molecules fell within the range of 0.99 to 0.83, suggesting that all the sensitizers produced comparable levels of photocurrent, and exhibited a degree of similarity in their performance. Based on the findings on the electronic excitation properties of the dyes (Table 4), the performance of the following four specific dyes was evaluated: DTP/POM, DBTP/POM, SN5/POM, and TD/POM.

The value of LHE indicated that the different donor systems can affect the LHE. Another factor enhancing  $J_{sc}$  was  $\varphi_{\text{inject}}$ , which pertains to the driving force ( $\Delta G_{\text{inject}}$ ) for the electron injection from the photo-induced excited states of the organic dyes to the  $\text{TiO}_2$  surface. Generally, a greater  $\Delta G_{\text{inject}}$



Table 4 The  $E_{\text{OX}}^{\text{dye}a}$ ,  $E_{\text{OX}}^{\text{dye}^*b}$ , LHE<sup>c</sup>,  $\Delta G_{\text{inject}}^d$ ,  $\Delta G_{\text{reg}}^e$ ,  $\Delta G_{\text{cr}}^f$  and  $V_{\text{OC}}^g$  of the studied hybrids

Dye	$E_{\text{OX}}^{\text{dye}}$ (eV)	$E_{\text{OX}}^{\text{dye}^*}$ (eV)	LHE	$\Delta G_{\text{inject}}$ (eV)	$\Delta G_{\text{reg}}$ (eV)	$\Delta G_{\text{cr}}$	$V_{\text{OC}}$ (V)
DTP/POM	<b>5.17</b>	<b>2.29</b>	<b>0.87</b>	<b>-1.71</b>	<b>-0.37</b>	<b>1.17</b>	<b>1.6</b>
<i>N</i> -Acyl/POM	5.4	2.72	0.97	-1.28	-0.6	1.4	1.49
PBTZ/POM	5.7	2.77	0.96	-1.23	-0.9	1.7	1.1
NPTA/POM	5	2.32	0.99	-1.68	-0.2	1	1.56
<b>DBTP/POM</b>	<b>5.6</b>	<b>2.44</b>	<b>0.834</b>	<b>-1.56</b>	<b>-0.8</b>	<b>1.6</b>	<b>1.55</b>
<b>SN5/POM</b>	<b>5.03</b>	<b>2.45</b>	<b>0.98</b>	<b>-1.55</b>	<b>-0.23</b>	<b>1.03</b>	<b>1.55</b>
SN6/POM	5.55	3	0.99	-1	-0.75	1.55	1.58
DTPO/POM	5.64	2.63	0.95	-1.37	-0.84	1.64	1.58
BDTP/POM	5.3	2.69	0.99	-1.31	-0.5	1.3	1.23
<b>TD/POM</b>	<b>6</b>	<b>3.34</b>	<b>0.98</b>	<b>-0.66</b>	<b>-1.2</b>	<b>2</b>	<b>1.45</b>
BTI/POM	6.4	3.57	0.90	-0.43	-1.6	2.4	0.88
TBI/POM	6.33	3.72	0.99	-0.28	-1.53	2.33	1.34

<sup>a</sup>  $E_{\text{OX}}^{\text{dye}}$  = redox potential of the ground state. <sup>b</sup>  $E_{\text{OX}}^{\text{dye}^*}$  = oxidation potential of the dye. <sup>c</sup> LHE = light harvesting efficiency. <sup>d</sup>  $\Delta G_{\text{inject}}$  = free energy change for electron injection. <sup>e</sup>  $\Delta G_{\text{reg}}$  = driving force of regeneration. <sup>f</sup>  $\Delta G_{\text{cr}}$  = charge recombination. <sup>g</sup>  $V_{\text{OC}}$  = the open-circuit photovoltage.

corresponds to a larger  $\varphi_{\text{inject}}$ . The synthesized dyes exhibited negative  $\Delta G_{\text{inject}}$  values, indicating that they possessed sufficient thermodynamic potential that facilitated the electron injection process. The value for DTP/POM was more negative than the others.

$J_{\text{sc}}$  is also affected by the efficiency of dye regeneration ( $\eta_{\text{reg}}$ ), which is influenced by the regeneration driving force,  $\Delta G_{\text{reg}}$ . From Table 4, the values for DTP/POM, DBTP/POM, SN5/POM, and TD/POM are 0.37, 0.8, 0.23, and 1.2 respectively. The  $\Delta G_{\text{cr}}$  values also indicate an inhibition of recombination. The calculated open-circuit voltage ( $V_{\text{OC}}$ ) values ranged from 1.45 to 1.6. As a result, TD/POM, SN5/POM, DTP/POM, and DBTP/POM can act as the most efficient sensitizers for dye-sensitized solar cells. It has been observed that the LHE and  $V_{\text{OC}}$  of these systems are comparable and exceed those of other sensitizers documented in the literature.<sup>45,46</sup>

## Conclusions

In this study, we investigated various POM-based hybrid dyes featuring electron-donating and electron-withdrawing groups, utilizing DFT and TD-DFT methods for assessing their potential applications as dyes in DSSCs. In the designed hybrids, the DPT-derived building blocks served as donor components, while the Keggin-type POM functioned as the acceptor moiety.

The initial investigation focused on the photophysical characteristics of the dyes. Among the designed hybrid dyes, SN6/POM and BDTP/POM exhibited a larger oscillator strength ( $f$ ) in the visible region, whereas TD/POM, SN5/POM, DTP/POM, and DBTP/POM demonstrated the highest CT character. The parameters associated with the intramolecular CT indicate that TD/POM, SN5/POM, DTP/POM, and DBTP/POM demonstrated a larger separation between the hole center and the electron compared to SN6/POM and BDTP/POM. The  $C_{\text{hole}}$  and  $C_{\text{ele}}$  map illustrates this hole-electron separation.

To assess the recombination rates of the holes (positive charge) and electrons (negative charge), the coulomb energy between the holes and the electrons was evaluated. The findings revealed that this energy for TD/POM, SN5/POM, DTP/POM, and

DBTP/POM was lower compared to SN6/POM and BDTP/POM, suggesting a potential for enhanced energy-conversion efficiency. The heat maps indicate that in the compounds DTP/POM, DBTP/POM, SN5/POM, and TD/POM, the organic ligand played a major role in hole contribution, while the inorganic POM was mainly responsible for electron contribution, indicating an LMCT-type electron transfer.

The analysis shows that the LUMO energy levels of the studied systems were consistently higher than the conduction band edge energy of  $\text{TiO}_2$ , making these systems well-suited for applications involving electron transfer in DSSCs. In contrast, the HOMO energy levels of these systems are more negative than the  $\text{I}^-/\text{I}_3^-$  redox potential, which is a critical factor for effective CT in n-DSSCs. Therefore, this alignment meets the necessary criteria for dyes used in these solar cells.

The study highlights the LHE values of the designed systems, with TD/POM and SN5/POM showing the highest efficiency of roughly 0.98. This suggests that the choice of donor materials significantly influences the LHE, and it is crucial for optimizing the performance of organic dye-sensitized solar cells. The synthesized hybrid dyes exhibit negative  $\Delta G_{\text{inject}}$  values, indicating that there was a favorable thermodynamic potential for electron injection, with DTP/POM demonstrating the most negative value, suggesting superior electron injection capabilities.

Additionally,  $J_{\text{sc}}$  was influenced by dye regeneration efficiency ( $\eta_{\text{reg}}$ ), which was determined by the regeneration driving force ( $\Delta G_{\text{reg}}$ ). The values for DTP/POM, DBTP/POM, SN5/POM, and TD/POM indicate that DBTP/POM and TD/POM had higher regeneration driving forces, potentially enhancing their overall performance. The open-circuit voltage ( $V_{\text{OC}}$ ) values ranged from 1.45 to 1.6, emphasizing the potential of these systems in solar energy applications.

## Author contributions

The study conception and design, calculation, data collection and analysis were performed by Maryam Fallah, Bahram Yadollahi, and Reza Omidyan. The first draft of the manuscript



was written by Maryam Fallah and Maryam Fallah, Bahram Yadollahi, and Reza Omidyan read and approved the final manuscript.

## Conflicts of interest

There are no conflicts to declare.

## Data availability

All data and information regarding materials in this paper are available in the article and the supplementary information (SI). Supplementary information is available. See DOI: <https://doi.org/10.1039/d5ra06975k>.

## Acknowledgements

The authors are thankful to the University of Isfahan for financially supporting this research.

## Notes and references

- 1 M. Freitag, J. Teuscher, Y. Saygili, X. Zhang, F. Giordano, P. Liska, J. Hua, S. M. Zakeeruddin, J.-E. Moser, M. Grätzel and A. Hagfeldt, *Nat. Photonics*, 2017, **11**, 372.
- 2 S. Prasanthkumar and L. Giribabu, *Curr. Sci.*, 2016, **111**, 1173.
- 3 M. A. Green, *Phys. E Low-dimens. Syst. Nanostruct.*, 2002, **14**, 65.
- 4 Z. Yao, M. Zhang, H. Wu, L. Yang, R. Li and P. Wang, *J. Am. Chem. Soc.*, 2015, **137**, 3799.
- 5 B. O'Regan and M. Grätzel, *Nature*, 1991, **353**, 737.
- 6 K. Kalyanasundaram and M. Grätzel, *Coord. Chem. Rev.*, 1998, **177**, 347.
- 7 L. V. Pugolovkin, S. Y. Vassiliev, M. I. Borzenko, V. K. Laurinavichyute and G. A. Tsirlina, *Russ. Chem. Bull.*, 2013, **62**, 1317.
- 8 S. Wu, C. Zhao, Y. Dong and L. Yan, *Polyoxometalates*, 2024, **3**, 9140070.
- 9 M. T. Pope and A. Müller, *A. Polyoxometalates, from Platonic Solids to Anti-retroviral Activity*, Kluwer Academic Publishers, 1994.
- 10 J. Zhi, X. Xu, S. Duan, W. Chen, F. Li, X. Guo and Y. Hou, *Eur. J. Inorg. Chem.*, 2023, **26**, e202200599.
- 11 C. L. Hill, *J. Mol. Catal. A: Chem.*, 2007, **262**, 2.
- 12 N. I. Gumerova and A. Rompel, *Nat. Rev. Chem.*, 2018, **2**, 0112.
- 13 J. B. Strong, G. P. A. Yap, R. Ostrander, L. M. Liable-Sands, A. L. Rheingold, R. Thouvenot, P. Gouzerh and E. A. Maatta, *J. Am. Chem. Soc.*, 2000, **122**, 639.
- 14 T. Zhang, W. Guan, S. Wen, T. Ma, L. Yan and Z. Su, *J. Phys. Chem. C*, 2014, **118**, 29623.
- 15 X. Luo, F. Li, B. Xu, Z. Sun and L. Xu, *J. Mater. Chem.*, 2012, **22**, 15050.
- 16 M. Lu, B. Xie, J. Kang, F.-C. Chen, Y. Yang and Z. Peng, *Chem. Mater.*, 2005, **17**, 402.
- 17 X. Sang, J. Li, W. Chen and E. Wang, *Mater. Lett.*, 2012, **87**, 39.
- 18 Y. Li, T. Pullerits, M. Zhao and M. Sun, *J. Phys. Chem. C*, 2011, **115**, 21865.
- 19 X. Wu, T. Huang, X. Tong, Z. Xie, W. Chen, Q. Wu and W. Yan, *RSC Adv.*, 2015, **5**, 21973.
- 20 J. Chen and Y. Cao, *Acc. Chem. Res.*, 2009, **42**, 1709.
- 21 F. P. V. Koch, M. Heeney and P. Smith, *J. Am. Chem. Soc.*, 2013, **135**, 13699.
- 22 L. Zhang, N. S. Colella, F. Liu, S. Trahan, J. K. Baral, H. H. Winter, S. C. Mannsfeld and A. L. Briseno, *J. Am. Chem. Soc.*, 2013, **135**, 844.
- 23 E. Zhou, K. Hashimoto and K. Tajima, *Polymer*, 2013, **54**, 6501.
- 24 S. C. Rasmussen, S. J. Evenson and C. B. McCausland, *Chem. Commun.*, 2015, **51**, 4528.
- 25 J. M. Maestre, X. Lopez, C. Bo, J. M. Poblet and N. Casan-Pastor, *J. Am. Chem. Soc.*, 2001, **123**, 3749–3758.
- 26 J. Zhang, H.-B. Li, S.-L. Sun, Y. Geng, Y. Wu and Z.-M. Su, *J. Mater. Chem.*, 2012, **22**, 568.
- 27 C. Lee, W. Yang and R. G. Parr, *Phys. Rev. B: Condens. Matter Mater. Phys.*, 1988, **37**, 785.
- 28 J. Autschbach, *ChemPhysChem*, 2009, **10**, 1757.
- 29 J. M. Poblet, X. López and C. Bo, *Chem. Soc. Rev.*, 2003, **32**, 297.
- 30 B. Moradpour and R. Omidyan, *RSC Adv.*, 2022, **12**, 34217–34225.
- 31 B. Moradpour and R. Omidyan, *Phys. Chem. Chem. Phys.*, 2025, **27**, 21526–21543.
- 32 S. Mir, B. Yadollahi and R. Omidyan, *J. Solid State Chem.*, 2022, **305**, 122667.
- 33 J. T. B. Mennucci and R. Cammi, *Chem. Rev.*, 2005, **105**, 2999e3094.
- 34 T. Lu and F. Chen, *J. Comput. Chem.*, 2012, **33**, 580.
- 35 S. Mir, B. Yadollahi, R. Omidyan and G. Azimi, *RSC Adv.*, 2020, **10**, 33718–33730.
- 36 T. Yanai, D. P. Tew and N. C. Handy, *Chem. Phys. Lett.*, 2004, **393**, 51.
- 37 N. Wazzan, *Processes*, 2025, **13**, 418.
- 38 Z. Xu, Y. Li, Y. Li, S. Yuan, L. Hao, S. Gao and X. Lu, *Spectrochim. Acta, Part A*, 2020, **233**, 118201.
- 39 C. A. Guido, P. Cortona, B. Mennucci and C. Adamo, *J. Chem. Theory Comput.*, 2013, **9**, 3118.
- 40 T. Le Bahers, C. Adamo and I. Ciofini, *J. Chem. Theory Comput.*, 2011, **7**, 2498.
- 41 M. Huix-Rotllant, M. Filatov, S. Gozem, I. Schapiro, M. Olivucci and N. Ferré, *J. Chem. Theory Comput.*, 2013, **9**, 3917.
- 42 Y. Gao, W. Guan, X.-S. Wang, R. Jia, L.-K. Yan and Z.-M. Su, *Phys. Chem. Chem. Phys.*, 2020, **22**, 16032.
- 43 Z. Ning, Y. Fu and H. Tian, *Energy Environ. Sci.*, 2010, **3**, 1170.
- 44 P. Qin, X. Yang, R. Chen, L. Sun, T. Marinado, T. Edvinsson, G. Boschloo and A. Hagfeldt, *J. Phys. Chem. C*, 2007, **111**, 1853.
- 45 H. Wu, T. Zhang, C. Wu, W. Guan, L. Yan and Z. Su, *Dyes Pigm.*, 2016, **130**, 168.
- 46 J. Wang, S. Cong, S. Wen, L. Yan and Z. Su, *J. Phys. Chem. C*, 2013, **117**, 2245.

